Integrated Ferroelectrics, 131:36–46, 2011

ISSN: 1058-4587 print / 1607-8489 online
DOI: 10.1080/10584587.2011.616400

Taylor & Francis
Taylor & Francis Group

Magnetoelectronics at Edges in Semiconductor Structures: Helical Aharonov-Casher Edge States

L. L. XU, SHAOLA REN, AND J. J. HEREMANS*

Virginia Tech, Department of Physics, Blacksburg, VA 24061, USA

It is shown that an Aharonov-Casher vector potential in a two-dimensional geometry can lead to helical edge states, and initial experimental results are presented. The Aharonov-Casher vector potential is the electromagnetic dual of the magnetic vector potential, and leads to traveling states at the sample edge in analogy to the integer quantum Hall effect. The helical edge states are predicted to appear in a narrow channel geometry with parabolic or sufficiently symmetric confinement potential. The present work discusses implications of the helical Aharonov-Casher edge states, experimental considerations in specific materials systems, and experimental quantum transport results in mesoscopic geometries.

The quantum Hall effects, both fractional and integer, occur in two-dimensional (2D) carrier systems upon application of a magnetic field $\boldsymbol{B}$ normal to the carrier plane [1, 2]. A description of the integer quantum Hall effect (IQHE) starts with the introduction of a magnetic vector potential, describing the interaction between a charge and a magnetic field. We consider here the physical phenomena generated by replacing the magnetic vector potential by the Aharonov-Casher (AC) vector potential (defined below) describing the interaction between a magnetic moment or spin and an electric field. The AC vector potential is an expression of spin-orbit interaction (SOI) and, linking magnetic moments and electric fields, is of deep but relatively unexplored importance in the quest for electrical manipulation of electron spin states (spintronics) and in magnetoelectronics. The present work studies one fundamental aspect of the AC vector potential. A sample edge necessarily is defined by an electric field, and one can ask what phenomena are induced on spins or magnetic moments at a sample edge by the AC vector potential. We find that in a narrow channel geometry the AC vector potential creates edge states that are electromagnetically dual to the IQHE edge states. The AC states are helical, akin, but not necessarily identical, to those characterizing the quantum spin Hall effect (QSHE) state [3–8]. In a thought experiment, we construct the following situation. The IQHE effect requires an applied magnetic field. Let us consider an observer in a moving inertial frame, with a velocity relative to the 2D carrier system such that the applied magnetic field is in this frame reduced to zero, according to the Lorentz transformation for electromagnetic fields. If the observed magnetic field is zero, what then is observed from the moving frame? We derive below that from a moving frame, in a mesoscopic narrow-channel geometry one can observe the helical AC edge states.

Received in final form June 25, 2011.
*Corresponding author. E-mail: heremans@vt.edu

The IQHE can be described as arising from one-dimensional (1D) states at the edges of a 2D system, in which backscattering is forbidden [9, 10]. The edge states arise from a broken translational invariance induced by the edge, lifting the Landau level degeneracy and leading to propagating chiral edge states. The chirality implies that states propagating in opposite directions are found at opposite sample sides, with the spatial separation protecting the states from backscattering. The protection results in quantization of the Hall conductivity σ_{xy} and vanishing longitudinal resistance. The QSHE state and its three-dimensional topological insulator analogs [3–8] have attracted considerable attention for the implications of their topologically protected states. As the IQHE, the QSHE occurs at the edge of a 2D system, but its 1D edge states show a spin structure [3, 5]. Unlike in the IQHE where spin polarity does not affect edge state propagation direction, in the QSHE opposite spin polarities at the same edge propagate in opposite directions (helical edge states). The spin-polarized channels are protected from scattering unless time-reversal symmetry is broken, flipping the spin and leading to backscattering within one edge [3]. We will see that, substituting spin for magnetic moments, such structure is also realized in a thought experiment whereby a moving witness observes the IQHE in a narrow channel.

As depicted in Fig. 1a, an observer in the frame $O(x,y,z)$ performs an IQHE experiment by applying $\boldsymbol{B} = (0,0,B)$ along the z-axis, normal to a 2D system situated in the x-y plane. To derive IQHE edge states in O, a potential describing the sample edges must be introduced [10, 11]. With the edge parallel to the x-axis, we use a parabolic confinement [11–13], $V(x,y) = \frac{1}{2}m\omega_p^2 y^2$. Hence a confinement electric field $\boldsymbol{\varepsilon} = (0,\varepsilon,0)$ is present on both sides of the sample, with a y-component linear in y, $\varepsilon = -(m/q)\ {\omega_p}^2\ y$ (carrier charge and mass are represented by q and m). The observer in O solves for $H_{AB}\ \boldsymbol{\Psi}(x,y) = E\boldsymbol{\Psi}(x,y)$ with:

$$H_{AB} = \frac{1}{2m}\,(\boldsymbol{p} - q\boldsymbol{A})^2 + \frac{1}{2}m\omega_p^2 y^2 \tag{1}$$

where $\boldsymbol{A}$ denotes the vector potential, for instance in the gauge $\boldsymbol{A} = \frac{1}{2}\ \boldsymbol{B} \times \boldsymbol{r}$ with $\boldsymbol{r}$ in the x-y plane. The $\boldsymbol{\Psi}(x,y)$ solving H_{AB} describe the known magnetic edge states

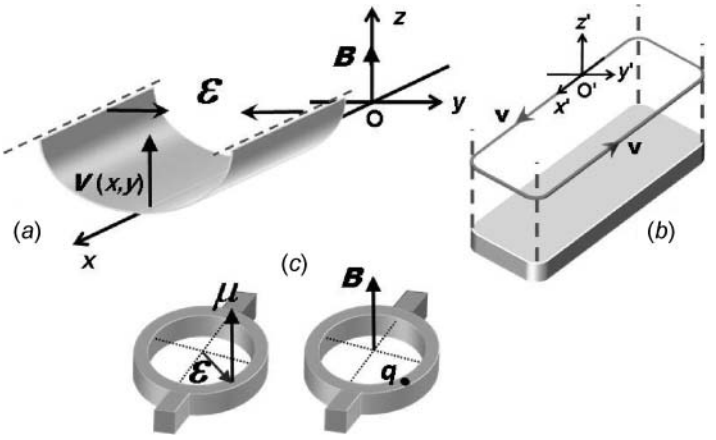

Figure 1. (a) The narrow wire in which the IQHE is set up, with parabolic potential at the edges, and coordinate frame O. (b) The coordinate frame O', and the schematic trajectory with velocity $\boldsymbol{v}$ followed by the moving observer in the thought experiment. (c) The duality between the AB effect induced by $q\boldsymbol{A}$ and the AC effect induced by $(1/c^2)\ \boldsymbol{\mu} \times \boldsymbol{\varepsilon}$, illustrated by interferometric ring geometries.

[10, 11]. In a thought experiment (in free space), another observer, attached to frame $O'(x',y',z')$, moves at velocity $\boldsymbol{v} = c^2(\boldsymbol{\varepsilon} \times \boldsymbol{B})/\varepsilon^2$ relative to O along the x-axis (Fig. 1b), where c is the speed of light. Assuming $q > 0$, in the thought experiment O' follows the edges defined by $\boldsymbol{\varepsilon}$ in a counter-clockwise path, since $v = -c^2\,B/\varepsilon$ for $y > 0$ and $v = c^2\,B/\varepsilon$ for $y < 0$ (the small segments parallel to the x-axis at the sample ends can be readily included without altering the conclusions below). Using the Lorentz transformation with the given $\boldsymbol{v}$, the observer in O' finds for $\boldsymbol{B}'$ and $\boldsymbol{\varepsilon}'$ in frame O', the following values: $\boldsymbol{B}' = (0,0,0)$ and $\boldsymbol{\varepsilon}' = (0,\ \varepsilon\ \sqrt{}(1 - (v/c)^2),\ 0)$. If $\boldsymbol{B}' = \boldsymbol{0}$, what then does O' observe concerning the IQHE edge states observed in O? The question is not trivial since the quantization of σ_{xy} in the IQHE can be expressed in terms of a topologically protected Chern number [14, 15, 8], and one may reasonably expect the Lorentz transformation to preserve topological protection in some form. It is thus expected that the moving observer still notices edge phenomena. We note that the presence of the edge, with its confinement $\boldsymbol{\varepsilon}$, plays an important role and that $\boldsymbol{\varepsilon} \perp \boldsymbol{B}$. We will see that the IQHE edge states are perceived by O' as edge states of magnetic moments (in a semiclassical thought experiment, since spin is distinct from classical moments, and specific phenomena arise from spin, such as the helicity of states in the QSHE). We point out that, notwithstanding classical limitations, thought-experiments using the Lorentz transformation point to a mapping that may help in the description of other edge phenomena, since in principle the transformation converts between different types of topologically non-trivial edge states. As example, beyond the scope of this paper, one may ask what a moving observer will conclude about the fractional quantum Hall effect [16]. Returning to the thought experiment, classically, the moving observer O' will perceive a magnetic moment $\boldsymbol{\mu} = \frac{1}{2}q\boldsymbol{r} \times \boldsymbol{v}$, generated by the charges q moving at velocity $\boldsymbol{v}$. Using $\boldsymbol{B} = (1/c^2)\ \boldsymbol{v} \times \boldsymbol{\varepsilon}$, observer O' then experiences $q\boldsymbol{A}$ as $q\boldsymbol{A} = (1/c^2)\ \boldsymbol{\mu} \times \boldsymbol{\varepsilon}$. Observer O' hence solves for $H_{AC}\ \Psi(x,y) = E\Psi(x,y)$ with:

$$H_{AC} = \frac{1}{2m}\left(\boldsymbol{p} - \frac{1}{c^2}\boldsymbol{\mu} \times \boldsymbol{\varepsilon}\right)^2 + \frac{1}{2}m\omega_p^2 y^2 \tag{2}$$

where we henceforth drop the primes for ease of notation. We notice the appearance in Eq. 2 of the Aharonov-Casher (AC) vector potential $(1/c^2)\ \boldsymbol{\mu} \times \boldsymbol{\varepsilon}$, generated by a pure electric field. Whereas the Aharonov-Bohm (AB) effect [17] describes the phase accumulated by a charged particle along a trajectory that encloses a magnetic field flux, its electromagnetic dual, the AC effect [18] describes the phase accumulated by a magnetic moment along a trajectory in an electric field. The duality [19] is schematically illustrated in the interferometric ring geometries of Fig. 1c, as would be used to detect the effects in mesoscopic experiments. Figure 2 shows an experimental realization of a ring for the measurement of the AB effect. The ring, in this sample of diameter 700 nm, was fabricated by electron-beam lithography and reactive ion etching on a two-dimensional electron system (2DES) contained in the InGaAs quantum well of an InGaAs/InAlAs semiconductor heterostructure. In the darker areas the InGaAs quantum well is etched away, and these areas form inaccessible barriers for the electrons. The electronically conducting path through the ring is schematically indicated by fine lines in Fig. 2, illustrating the correspondence with Fig. 1c (right). Application of $\boldsymbol{B}$ creates a magnetic flux threading the ring and generates the AB quantum phase, with a resulting interference effect measurable by low-temperature (<5 K) quantum transport. Experimental examples will be presented below. The AC effect itself was experimentally confirmed using neutron beam interferometry [20]. In the solid-state its similarity to the materials property of SOI has led to experiments [21–23] and theoretical work [24–26]. Expressions of the duality based on the Dirac equation were presented in

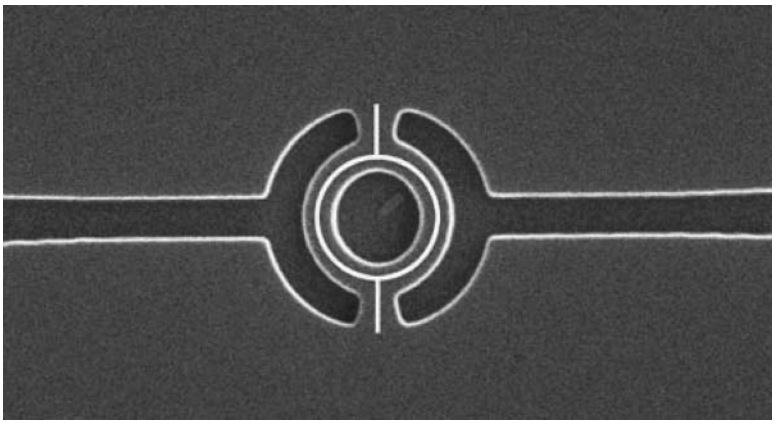

Figure 2. SEM micrograph of an experimental realization, by electron-beam lithography and reactive ion etching, of a ring for the measurement of the AB effect in an InGaAs/InAlAs semiconductor heterostructure. The electronically conducting path through the ring is schematically indicated by fine lines. The darker areas represent etched regions, forming barriers for the electrons. The ring has average diameter of 700 nm, and lithographic arm width of 300 nm.

Ref. 27. The Landau-like levels induced by the AC vector potential for various profiles of $\boldsymbol{\varepsilon}$ were described in Ref. 28.

We can now ask about the generality of the thought experiment, since both the flight path and velocity of O' seem specific. Concerning the path, all edges yield the same H_{AC} if one or several independent observers O' (one for each edge) consistently adhere to $\boldsymbol{v}$. The conclusions below will hence be valid over all edges along the entire sample perimeter. Concerning the magnitude $v = c^2\, B/\varepsilon$, in the thought experiment it was chosen to yield a pure electric field in frame O', whereas $v = 0$ yields a pure magnetic field. We thus have two endpoints of a series of relativistically correspondent phenomena: H_{AB} describing q in applied $\boldsymbol{B}$, and H_{AC} describing μ in applied $\boldsymbol{\varepsilon}$. Once O and O' are established as inertial frames, we can of course disregard the origin of H_{AB} and H_{AC} from the thought experiment and solve H_{AB} and H_{AC} in the local frame. Intermediate velocities will yield various ratios of perpendicular $\boldsymbol{\varepsilon}$ and $\boldsymbol{B}$. It follows that applied mixed $\boldsymbol{\varepsilon}$ and $\boldsymbol{B}$ likely also yield non-trivial edge phenomena, although the resulting states are not the topic of this paper. We now turn our attention to solving H_{AC}.

In Eq. 2 and in Fig. 1a-c, we consider for now $\boldsymbol{\mu}//\boldsymbol{z}$, such that $\boldsymbol{\mu} = (0,0,\mu_z)$. We will be able to relax this requirement later, since only the product $\boldsymbol{\mu} \times \boldsymbol{\varepsilon}$ is involved. We introduce $\omega_A = \mu_z \omega_p^2/(qc)^2 = \frac{1}{2}\, \omega_p\, (\mu_z/\mu_\mathrm{B})\, (\hbar\omega_p/mc^2)$ with μ_B the Bohr magneton. Here ω_A holds the same role in H_{AC} as the cyclotron frequency $\omega_C = qB/m$ holds in H_{AB}. Using a wave function localized in y and with plane-wave nature along x over a sample of length L, $\boldsymbol{\Psi}(x,y) = (1/L)^{1/2}\, \mathrm{e}^{ikx}\zeta(y)$, we obtain for the transverse function $\zeta(y)$:

$$\left[\frac{1}{2m}\,(\hbar k - m\omega_A y)^2 + \frac{p_y^2}{2m} + \frac{1}{2}m\omega_p^2 y^2\right]\zeta(y) = E\zeta(y) \tag{3}$$

which, using a procedure identical to that yielding edge states in the IQHE [10, 11], can be rewritten as a harmonic oscillator shifted in y:

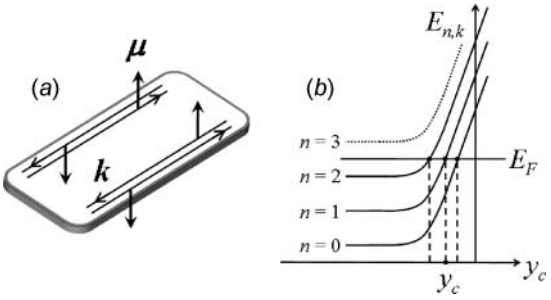

Figure 3. (a) Schematic depiction of the helical edge states induced by the AC vector potential. If at a given edge the signs of $\boldsymbol{k}$ and μ_z are changed simultaneously, the location of the edge state does not change. Counterpropagating states of opposite μ_z but same n are in fact superposed. (b) Schematic depiction of $E_{n,k}$ as function of the wave function center point y_c. As in the IQHE, propagating states (labeled by n, k and here also μ_z) exist at y-coordinates where E_F intersects $E_{n,k}$.

$$\left[\lambda\frac{\hbar^2k^2}{2m}+\frac{p_y^2}{2m}+\frac{1}{2}m\Omega^2\,(y-\eta k)^2\right]\zeta(y)=E\zeta(y) \tag{4}$$

with $\lambda=\omega_p{}^2/(\omega_p{}^2+\omega_A{}^2)$, $\Omega=(\omega_p{}^2+\omega_A{}^2)^{1/2}$ and $\eta=\mathrm{h}\omega_A\,/\,[m(\omega_p{}^2+\omega_A{}^2)]$. We find that the energy, $E_{n,k}=\lambda(\hbar^2k^2)/(2m)+\hbar\Omega\,(n+1/2)$, and that $\zeta_{n,k}(y)=\mathrm{e}^{-q2/2}\,H_n(q)$ with $q=y-\eta k$ and with $H_n(q)$ the n^{th} Hermite polynomial. The transverse wave function is hence centered at $y_c=\eta\,k$. A similar spatial separation was derived in the context of spin accumulation at the boundaries under confinement-induced SOI [12, 29, 30] (*cfr* below) or in the context of quantized magnetization transport [31]. However, given the mapping of Eqs. 2–4 on IQHE equivalents, an analysis in terms of edge states is compelling. The velocity of the state is $(1/\hbar)(\mathrm{d}E_{n,k}/\mathrm{d}k)=\lambda\,(\hbar k/m)$. The position $y_c=\eta k$ and the velocity are hence both proportional to k. Yet, y_c also depends on μ_z, via ω_A. To conclude the same position y_c and same energy $E_{n,k}$ for given states, the signs of k and μ_z must be changed simultaneously. Hence at the same edge, states with $\mu_z>0$ propagate in a direction opposite to states with $\mu_z<0$, as illustrated in Fig. 3a. Figure 3b schematically depicts the energy dispersion close to the edge. At the edge, the Fermi level E_F cuts through a finite number of dispersion curves $E_{n,k}$, labeled by n, at their respective locations y_c, with higher n corresponding to locations further removed from the edge. In the bulk the $E_{n,k}$ develop a gap, in analogy with Landau levels generating edge states in the IQHE. Equations 2–4 apply for an arbitrary μ, and in particular applies for the moment from a particle of spin 1/2. In that case, $\mu_z>0$ and $\mu_z<0$ are naturally identified with the two projections of the spin along the quantization axis [26, 32]. In the case of spin 1/2, after solving Eqs. 2–4, an observer will hence conclude to the existence of helical edge states, as depicted in Fig. 3a. Helical edge states (based on the projection of spin in the z-direction) are also found in the QSHE [3, 5]. Backscattering at one edge in Fig. 3a requires $\boldsymbol{\mu}$ to be flipped, $\mu_z\rightarrow-\mu_z$, an operation which, involving a magnetic quantity, requires time reversal symmetry to be broken. Hence, unless scattering potentials are present whereby time reversal symmetry is broken, an incident electron will be transmitted across disordered regions, and backscattering is suppressed as the temperature $T\rightarrow 0$. Thus the physical picture closely parallels the QSHE, and a similar reasoning emerges regarding measurable quantities [3]. The helical edge states here arise in a simple mesoscopic wire with parabolic confinement potential, under the action of the AC vector

potential, and do not require the special band structure under which the QSHE was so far described [3–8].

The electric field $\boldsymbol{\varepsilon}$ assumes two roles: the linearity of ε in y over the width of the sample leads to an AC vector potential equivalent to the magnetic vector potential of a homogeneous $\boldsymbol{B}$, and, the resulting parabolic $V(x,y)$ defines the sample's edges. The double role is illustrated by $\Omega = (\omega_p^2 + \omega_{\mathrm{A}}^2)^{1/2}$, where both ω_p and ω_A depend on the existence of the parabolic potential, whereas ω_C is independently created by $\boldsymbol{B}$ in the IQHE equivalent $\Omega = (\omega_p^2 + \omega_C^2)^{1/2}$. The need in Eq. 2 to maintain $\boldsymbol{\varepsilon}$ across the sample width indicates a particular relevance for narrow channels, such as encountered in mesoscopic experiments and point-contacts. The energy gap $\hbar\Omega$ yields an insulating bulk when E_F lies within this gap, while the edges remain metallic (Fig. 3b). The gap isolates the edge states and plays an important role in the IQHE and QSHE. We should thus ascertain how deviations from parabolicity in $V(x,y)$ affect the isolation of the helical edge states. To first order, we find that a perturbation symmetric in y alters the magnitude of the gap but does not qualitatively affect the isolation of edge states. A perturbation asymmetric in y leads to a shift in $E_{n,k}$ (y_c) and can affect the isolation if of sufficient strength, establishing the benefits of a symmetric $V(x,y)$.

With a vector potential at hand in Eq. 2, we can now apply the Laughlin gauge-invariance argument for quantization of $\sigma_{xy} = ne^2/h$ (n an integer), in the IQHE [33, 10]. The argument can be appreciated in the light of the Maxwell-Faraday expression in Maxwell's equations: a temporal change in magnetic flux by the flux quantum h/e creates a current corresponding to the transport of a unit charge e. This results in a conductance quantized in e^2/h. Assuming constant $\boldsymbol{\mu}$, we find that now the AC cross line integral of $\boldsymbol{\varepsilon}$ ("AC flux") through Laughlin's cylinder (also in the rings of Fig. 1c) is quantized as:

$$\frac{1}{c^2}\boldsymbol{\mu} \cdot \oint \boldsymbol{\varepsilon} \times \boldsymbol{dl} = n2\pi\hbar \tag{5}$$

with n an integer. The role of e is assumed by the projection of μ normal to the plane of $\boldsymbol{\varepsilon}$ (*cfr* Fig 1c), μ_{n}. As can be seen from Eq. 5, the cross line integral of $\boldsymbol{\varepsilon}$ is quantized in units of $c^2\ h/\mu_{\mathrm{n}}$ and hence the role of the flux quantum h/e goes to $c^2\ h/\mu_{\mathrm{n}}$. The force on a magnetic moment can be expressed as [34]:

$$F_\mu = \nabla(\boldsymbol{\mu} \cdot \boldsymbol{B}) - \frac{1}{c^2}\frac{d}{dt}(\boldsymbol{\mu} \times \boldsymbol{\varepsilon}) \tag{6}$$

After integrating over a contour, the second term expresses the additional force on μ due to a temporal change in the cross line integral of $\boldsymbol{\varepsilon}$ in Eq. 5, in analogy to the Maxwell-Faraday expression. Hence, we expect a transport of a magnetic moment μ_{n} in response to a temporal change in the cross line integral by the quantum $c^2\ h/\mu_{\mathrm{n}}$. This results in a magnetization conductance quantized in ${\mu_{\mathrm{n}}}^2/h$. The quantization of $\sigma_{xy} = n\ e^2/h$ in the IQHE is in the dual effect replaced by quantized magnetization transport (see also Refs. 3 and 31). Unlike e however, μ_{n} is not a universal constant, since values for μ, in the solid-state as well as for elementary particles, depend on interactions. Furthermore, in contrast to charge, magnetization is not a strictly conserved quantity. Thus, while the quantization is expected to occur, universal values are not anticipated. In the broadest terms, we recognize that the AC vector potential, when transformed from the magnetic vector potential, introduces phenomena at the edge of a narrow channel.

We now compare the results from Eqs. 2–4 to confinement-induced SOI. The SOI term in the Hamiltonian can be written as $H_{SO} = \beta\ \boldsymbol{\sigma} \cdot (\boldsymbol{k} \times \boldsymbol{\varepsilon})$, where $\boldsymbol{\sigma}$ is the vector of Pauli

matrices, and where $\boldsymbol{\varepsilon}$ is identified with the in-plane confinement electric field [12, 29, 35]. With the y-component of $\boldsymbol{\varepsilon}$ as $\varepsilon = -(m/q)\,\omega_p^2\,y$, with $\boldsymbol{k}//\boldsymbol{x}$ and considering the projection of spin along $\boldsymbol{z}$, we can write $H_{SO} = -\hbar\,k\,\omega_S\,y$. This defines ω_S, with a role equivalent to ω_A above. In analogy to Eq. 3 we find that the transverse function $\zeta(y)$ follows:

$$\left[\frac{\hbar^2k^2}{2m} - \hbar k\omega_S y + \frac{p_y^2}{2m} + \frac{1}{2}m\omega_p^2 y^2\right]\zeta(y) = E\zeta(y) \tag{7}$$

We rescale the potential term in Eq. 7 to a weaker confinement potential $\frac{1}{2}\,m\,\omega_p'^2\,y^2$ with $\omega_p'^2 = (\omega_p^2 - \omega_S^2)$ and recover a form identical to Eq. 3 with the substitution of $\omega_p \rightarrow \omega_p'$ (rescaling of the potential does not affect the physical conclusions). After rewriting Eq. 7 as a shifted harmonic oscillator, the energy is expressed as $E_{n,k} = \lambda'\,(\hbar^2k^2)/(2m) + \hbar\Omega'\,(n + 1/2)$, with $\lambda' = \omega_p'^2/(\omega_p'^2 + \omega_S^2)$, and $\Omega' = (\omega_p'^2 + \omega_S^2)^{1/2}$. The transverse wave function becomes $\zeta_{n,k}(y) = \mathrm{e}^{-q2/2}\,H_n(q)$ with $q = y - \eta'\,k$ where $\eta' = \hbar\omega_S/[m(\omega_p'^2 + \omega_S^2)]$. Hence $\zeta_{n,k}(y)$ is now centered at $y_c = \eta'\,k$. Equation 7, in complete analogy to Eq. 3, will then indeed yield spatially-separated helical edge states, counterpropagating for opposite spins. The helical edge states induced by H_{SO} are thus equivalent to the AC edge states. Such SOI states are of interest in mesoscopic geometries, particularly in split-gate point-contacts. A parabolic $V(x,y)$ with an in-plane $\boldsymbol{\varepsilon}$ however only approximates the complex three-dimensional $\boldsymbol{\varepsilon}$ encountered in split-gate point-contacts [13, 36]. For instance, a y-dependent z-component of $\boldsymbol{\varepsilon}$, $\boldsymbol{\varepsilon}_z(y)$, likely exists in these systems, in addition to the in-plane component of $\boldsymbol{\varepsilon}$. As mentioned above however, only $\boldsymbol{\mu} \times \boldsymbol{\varepsilon}$ matters, and with Bychkov-Rashba SOI [37, 38] aligning spin perpendicular to $\boldsymbol{k}$ and to $\boldsymbol{z}$, $\boldsymbol{\varepsilon}_z(y)$ can then lead to a term analogous to $-\hbar\,k\,\omega_S\,y$. We conclude that in point-contacts, either the y- or inhomogeneous z-component of $\boldsymbol{\varepsilon}$ can yield helical edge states, with implications for transport phenomena [39].

Next we outline experimental challenges to observe the helical states from Eqs. 2–4. We assume that the observer uses the electron spin for $\boldsymbol{\mu}$ and the confinement field for $\boldsymbol{\varepsilon}$. As described above for SOI, the term $\boldsymbol{\mu} \times \boldsymbol{\varepsilon}$ can in mesoscopic geometries either arise from the projections of spin along $\boldsymbol{z}$ (via ε_y) or along $\boldsymbol{y}$ (via $\varepsilon_z(y)$). To maximize μ and minimize the effective c, we consider the quasi-relativistic [40] narrow-gap semiconductors with large electron g-factors (g), InGaAs [32], InAs [41] or InSb [42–44]. The band structure implies a momentum vs energy response differing from that in vacuum, determining the electron dynamics under electromagnetic fields. Non-parabolicity in the conduction band can be expressed in terms of an effective $c \approx (E_g/2m^*)^{1/2}$, where E_g denotes the bandgap and m^* the effective mass at the Γ-point [40]. For InGaAs, InAs and InSb it is found that $c \approx 1.2{\times}10^6$ m/s, about 250 times lower than the vacuum value. The magnetic moment is considered as $\mu = \frac{1}{2}\,g\,\mu_\mathrm{B}$. As all three materials yield similar estimates, we consider a 2D system in InAs (Γ-point $m^* = 0.024\,m_e$ with m_e the free electron mass, and $g = -15$). At a 2D density 10^{12} cm^{-2}, taking non-parabolicity into account, $E_F = 83$ meV. To derive a value for ω_p, we use E_F as the approximate classical turning point of $V(x,y)$, and assume a depletion layer width of 0.15 μm at the edge, within the range of values encountered in 2D system (depletion layers in InSb 2DESs [44, 45] are wider than in InAs 2DESs [23], likely due to the accumulation layer present at InAs surfaces [46]). We find $\varepsilon \approx 10^6$ V/m (similar values of ε, about an order of magnitude below breakdown, are typical in semiconductor heterostructures, justifying the approach). With these values we find $\hbar\omega_A \approx 0.01$ meV, corresponding to 0.13 K. It is enlightening to cast this estimate in an IQHE equivalent: $\hbar\omega_A$ corresponds to ~ 7 mT in a GaAs 2DES IQHE experiment. The small energy gaps point to experimental challenges for experiments closely copying the

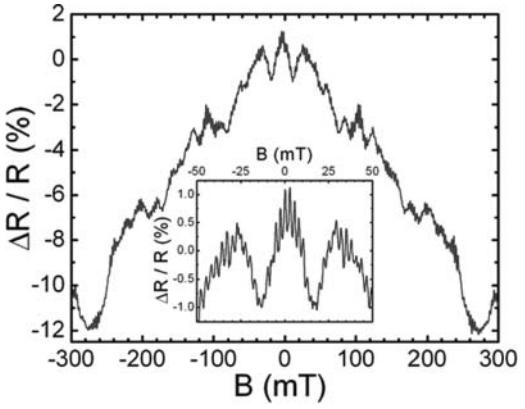

Figure 4. Magnetoresistance $\Delta R(B)$ at $T = 0.4$ K due to AB oscillations in a single ring fabricated on an InGaAs 2DES. The low-B inset shows the h/e period at higher resolution. Universal conduction fluctuations are responsible for the quasi-periodic broad maxima.

standard IQHE geometries, and suggest the interferometric mesoscopic ring experiments mentioned above, with their excellent spectroscopic resolution. Also, the dual effect predicts quantized magnetization transport (rather than charge, and not to fundamental constants). Direct measurement of magnetization transport creates experimental difficulties, partially avoidable by a conversion to electrical measurements. Equation 2 also predicts Shubnikov-De Haas-like oscillations in magnetotransport, from density-of-states effects. In the edge state regime, one can also envision measurements based on altering the edge state structure via side gates, or using applied magnetic fields to align $\boldsymbol{\mu}$ parallel to $\boldsymbol{\varepsilon}$.

The interest in spin control and spin edge phenomena renders experiments to test the reality of the AC edge states compelling, and we thus now turn to experimental efforts. As an illustration of interferometric measurements of quantum phase effects, Fig. 4 shows AB oscillations observed in an InGaAs 2DES single ring of average diameter of 1.4 μm and lithographic arm width 300 nm (the sample fabrication and layout follow Fig. 2). The 10 nm wide InGaAs quantum well containing the 2DES forms part of an InGaAs/InAlAs heterostructure, with electron density of 9.0×10^{15} m^{-2} and mobility 5.9 m^2/Vs at $T =$ 0.4 K. The heterostructure is asymmetrically doped with resulting dominant Bychkov-Rashba SOI [37, 38]. The electron quantum phase coherence length reaches several μm at $T = 0.4$ K, allowing phase-coherent experiments. The measurement consists of a sensitive 4-contact resistance measurement over the ring, at $T = 0.4$ K. The ring resistance oscillates as function of perpendicularly applied $\boldsymbol{B}$, with a periodicity corresponding to one magnetic flux quantum h/e threading the ring. The main figure indicates a magnetoresistance with a short-period oscillatory signal persisting with variable amplitude up to high $\boldsymbol{B}$, and riding on a quasi-periodic background. The inset magnifies the short-period signal, showing the period of 2.9 mT in close agreement with the expected h/e flux periodicity. The quasi-periodic background is representative of universal conductance fluctuations in quantum-coherent mesoscopic devices. Similar but electromagnetically dual interferometric measurements in semiconductor devices form the basis for the experimental pursuit of AC phases and AC edge states.

Figure 5 describes a sample structure to experimentally access AC phases and AC edge states. The sample was fabricated on the same material as the sample in Fig. 4, and was measured at $T = 1.2$ K in a $\boldsymbol{B}$ tilted at an angle to the 2DES normal. The geometry is a

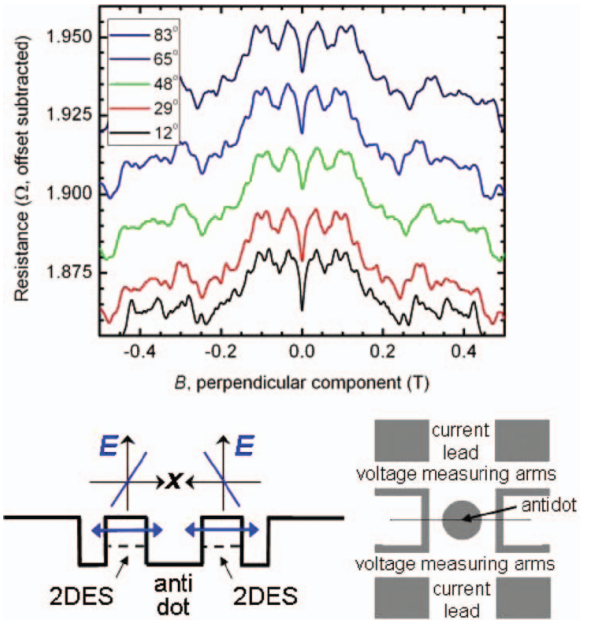

Figure 5. Top: Angular dependence of the magnetoresistance *vs* $B_\perp$ of a narrow InGaAs channel (1 μm width) with a quantum antidot (ø 300 nm) at 1.2 K (insert: θ values). *Bottom right*: Schematic of quantum antidot samples. Etched regions are dark. Voltage measurement arms and current leads are connected to electrical contacts. *Bottom left*: Horizontal cross-section through the sample, schematically showing conducting 2DES regions and in-plane confinement ε. A $\sim$ linear profile of ε in the channels implies a $\sim$ parabolic potential.

quantum antidot (QAD, an etched disc inaccessible for electrons, diameter 300 nm) in a narrow and short channel (width and length 1.0 μm) [47–52]. Samples did not have side- or top gates. The approximate profile of $\boldsymbol{\varepsilon}$ for the QAD sample is depicted in Fig. 5 (bottom left): we can assume a parabolic confinement potential (linear $\boldsymbol{\varepsilon}$) in the channels on the sides of the QAD, and a decaying $\boldsymbol{\varepsilon}$ in the direction of the current leads (Fig. 5, bottom right). The angle θ between $\boldsymbol{B}$ and the 2DES plane was varied from $\theta = 0^o$ (in-plane, $\boldsymbol{B}$ // measurement current) to $\theta = 90^o$ ($\boldsymbol{B} \perp$ 2DES), and the measured magnetoresistance plotted *vs* the normal component of $\boldsymbol{B}$, $B_n = B \sin[\theta]$. AB-type oscillations appear at low B, with multiple B_n periodicities (Fig. 5), due to closed paths less well defined than on ring geometries. When varying θ, fine structure appears in the magnetoresistance when the in-plane component of $\boldsymbol{B}$, $B_{//} = B \cos[\theta]$, is appreciable (e.g. $\theta < 48^o$, Fig. 5), in the moderate range of B_n studied (0.5 T). A low but non-zero $B_{//}$ results in time-reversal symmetry breaking via Zeeman splitting and coupling to the orbital motion in finite thickness quantum wells [53–55]. The effects are small here due to the comparatively strong Bychkov-Rashba SOI [37, 38] in our samples. Indeed, Bychkov-Rashba SOI corresponds to an in-plane effective $B \approx 3$ T, while $B_{//} < 0.5$ T. Varying θ results in a rotation of the total $\boldsymbol{B}$ experienced by the electrons (applied $\boldsymbol{B}$ plus effective in-plane $\boldsymbol{B}$ from Bychkov-Rashba SOI) and hence a rotation in the spin precession axis. This leads to a rotation in μ at each point along the paths and a change in $(1/c^2)\ \boldsymbol{\mu} \times \boldsymbol{\varepsilon}$, integrated over the interfering paths. The rotation is small ($<< \tan^{-1}[0.5/3] \approx 10^o$) at any point along the path, limited by the mostly in-plane spin direction and the moderate $B_{//}$. Effects of the AC phase are hence expected to be moderate

and smoothly varying in θ. Indeed, a moderate amplitude change is observed in Fig. 5. Yet, the fine structure at $\theta = 12^{o}$ cannot be ascribed to the AC phase and a more likely origin can be found in resonant tunneling effects [51, 52] between AC edge states formed on opposite edges of each of the two narrow side channels formed between the channel walls and the QAD. When the resonant tunneling condition is fulfilled, communication is established between AC edge states on opposite sides of the channel, resulting in a breakdown in the absence of backscattering and a measurable resistance change. The mT spacing for the fine structure in Fig. 5 is consistent with the expected approximate energy spacing between AC edge states, as derived above. Moreover, samples without the central QAD do not show fine structure, in agreement with the hypothesis that the QAD forms a resonant island which allows detection of AC edge states. We have also investigated channels with 5 QADs in series, and could not identify fine structure, as expected if averaging over variations in QAD diameter reduces the resonance peaks.

Beyond the preliminary QAD data presented here, samples are being designed to strengthen the demonstration of interferometric detection of Aharonov-Casher edge states. In conclusion, we address Aharonov-Casher edge states in a narrow channel. Helical edge states are predicted, which possess several features akin to the edge states in the recently-described QSHE. The vector potential transformation used in this work raises the possibility that other sets of closely-related effects may exist. Beyond fundamental interest, the Aharonov-Casher phenomena may also present avenues for electrical control of spin and magnetic moments in magnetoelectronics.

The authors are grateful for the high-quality InGaAs quantum well material provided by M. B. Santos from the University of Oklahoma. The authors acknowledge illuminating discussions with M. Rudolph, D. Minic, K. Park and V. Scarola. This work is supported by DOE through award DE-FG02-08ER46532.

References

1. K. von Klitzing, G. Dorda, and M. Pepper, *Phys. Rev. Lett.* **45**, 494 (1980).
2. D. C. Tsui, H. L. Stormer, and A. C. Gossard, *Phys. Rev. Lett.* **48**, 1559 (1982).
3. C. L. Kane, and E. J. Mele, *Phys. Rev. Lett.* **95**, 226801 (2005).
4. B. A. Bernevig, T. A. Hughes, and S. C. Zhang, *Science* **314**, 1757 (2006).
5. M. Koenig, S. Wiedemann, C. Brne, A. Roth, H. Buhmann, L. W. Molenkamp, X. L. Qi, and S. C. Zhang, *Science* **318**, 766 (2007).
6. L. Fu, C. L. Kane, and E. J. Mele, *Phys. Rev. Lett.* **98**, 106803 (2007).
7. J. E. Moore, and L. Balents, *Phys. Rev.* **B 75**, 121306(R) (2007).
8. (a) For reviews, see M. Koenig, H. Buhmann, L. W. Molenkamp, T. Hughes, C. X. Liu, X. L. Qi, and S. C. Zhang, *J. Phys. Soc. Jpn.* **77**, 031007 (2008); (b) M. Z. Hasan and C. L. Kane, *Rev. Mod. Phys.* **82**, 3045 (2010).
9. B. I. Halperin, *Phys. Rev.* **B 25**, 2185 (1982).
10. A. H. MacDonald, and P. Streda, *Phys. Rev.* **B 29**, 1616 (1984).
11. W. Zawadzki, Springer Series in Solid-State Sciences Vol. 87, *High magnetic fields in semiconductor physics II*, ed. G. Landwehr (Springer-Verlag Berlin Heidelberg, 1989).
12. K. Hattori, and H. Okamoto, *Phys. Rev.* **B 74**, 155321 (2006).
13. J. H. Hsiao, K. M. Liu, S. Y. Hsu, and T. M. Hong, *Phys. Rev.* **B 79**, 033304 (2009).
14. D. J. Thouless, M. Kohmoto, M. P. Nightingale, and M. den Nijs, *Phys. Rev. Lett.* **49**, 405 (1982).
15. Y. Hatsugai, *Phys. Rev. Lett.* **71**, 3697 (1993).
16. J. J. Heremans, and D. Minic, arXiv:0802.4117.
17. Y. Aharonov, and D. Bohm, *Phys. Rev.* **115**, 485 (1959).
18. Y. Aharonov, and A. Casher, *Phys. Rev. Lett.* **53**, 319 (1984).

19. R. Hagen, *Phys. Rev. Lett.* **64**, 2347 (1990).
20. A. Cimmino, G. I. Opat, A. G. Klein, H. Kaiser, S. A. Werner, M. Arif, and R. Clothier, *Phys. Rev. Lett.* **63**, 380 (1989).
21. T. Bergsten, T. Kobayashi, Y. Sekine, and J. Nitta, *Phys. Rev. Lett.* **97**, 196803 (2006).
22. M. Koenig, A. Tschetschetkin, E. M. Hankiewicz, J. Sinova, V. Hock, V. Daumer, M. Schaefer, C. R. Becker, H. Buhmann, and L. W. Molenkamp, *Phys. Rev. Lett.* **96**, 076804 (2006).
23. R. B. Lillianfeld, R. L. Kallaher, J. J. Heremans, Hong Chen, N. Goel, S. J. Chung, M. B. Santos, W. Van Roy, and G. Borghs, *Physics Procedia* **3**, 1231 (2010).
24. H. Mathur, and A. D. Stone, *Phys. Rev. Lett*. **68**, 2964 (1992).
25. A. V. Balatsky, and B. L. Altshuler, *Phys. Rev. Lett.* **70**, 1678 (1993).
26. X. F. Wang, and P. Vasilopoulos, *Phys. Rev.* B **72**, 165336 (2005).
27. Ya. I. Azimov, and R. M. Ryndin, *JETP Lett.* **61**, 454 (1995).
28. S. Bruce, *J. Phys.* A **38**, 6999 (2005).
29. Y. Jiang, and L. Hu, *Phys. Rev.* **B 74**, 075302 (2006).
30. Y. Xing, Q.-f. Sun, L. Tang, and J. Hu, *Phys. Rev.* **B 74**, 155313 (2006).
31. F. Meier, and D. Loss, *Phys. Rev. Lett.* **90**, 167204 (2003).
32. M. Kohda, T. Bergsten, and J. Nitta, *J. Phys. Soc. Japan* **77**, 031008 (2008).
33. R. B. Laughlin, *Phys. Rev.* **B 23**, 5632 (1981).
34. Y. Aharonov and D. Rohrlich, *Quantum paradoxes: quantum theory for the perplexed*, Wiley (2005), ISBN 978–3-527–40391-2, chapter 13.4.
35. P. Debray, S. M. S. Rahman, J. Wan, R. S. Newrock, M. Cahay, A. T. Ngo, S. E. Ulloa, S. T. Herbert, M. Muhammad, and M. Johnson, *Nature Nanotechnology* **4**, 759 (2009).
36. J. A. Nixon, J. H. Davies, and H. U. Baranger, *Phys. Rev.* **B 43**, 12638 (1991).
37. Y. A. Bychkov, and E. I. Rashba, *Journal of Physics* **C 17**, 6039 (1984).
38. R. Winkler, Springer Tracts in Modern Physics Vol. 191, *Spin-orbit coupling effects in two-dimensional electron and hole systems* (Springer-Verlag, Berlin Heidelberg, 2003).
39. A review can be found at: *J. Phys.: Condens. Matter* **20**, No. 16 (2008).
40. W. Zawadzki, S. Klahn, and U. Merkt, *Phys. Rev. Lett.* **55**, 983 (1985).
41. S. Brosig, K. Ensslin, and A. G. Jansen, *Phys. Rev.* B **61**, 13045 (2000).
42. R. L. Kallaher, and J. J. Heremans, *Phys. Rev.* B **79**, 075322 (2009).
43. R. L. Kallaher, J. J. Heremans, N. Goel, S. J. Chung, and M. B. Santos, *Phys. Rev.* **B 81**, 075303 (2010).
44. R. L. Kallaher, J. J. Heremans, N. Goel, S. J. Chung, and M. B. Santos, *Phys. Rev.* **B 81**, 035335 (2010).
45. Hong Chen, J. J. Heremans, J. A. Peters, N. Goel, S. J. Chung, and M. B. Santos, *Appl. Phys. Lett.* **86**, 032113 (2005).
46. D. C. Tsui, *Phys. Rev.* **B 12**, 5739 (1975).
47. J. A. Simmons, H. P. Wei, L. W. Engel, D. C. Tsui and M. Shayegan, *Phys. Rev. Lett.* **63**, 1713 (1993).
48. V. J. Goldman and B. Su, *Science* **267**, 1010 (1995).
49. A. S. Sachrajda, Y. Feng, R. P. Taylor, G. Kirczenow, L. Henning, J. Wang, P. Zawadzki and P. T. Coleridge, *Phys. Rev.* **B 50**, 10856 (1994).
50. V. J. Goldman, I. Karakurt, J. Liu and A. Zaslavsky, *Phys. Rev.* **B 64**, 085319 (2001).
51. I. Karakurt, V. J. Goldman, J. Liu and A. Zaslavsky, *Phys. Rev. Lett.* **87**, 146801 (2001).
52. V. J. Goldman, J. Liu and A. Zaslavsky, *Phys. Rev.* **B 77**, 115328 (2008).
53. F. E. Meijer, A. F. Morpurgo, T. M. Klapwijk, J. Nitta, *Phys. Rev. Lett.* **94**, 186805 (2005).
54. F. E. Meijer, A. F. Morpurgo, T. M. Klapwijk, T. Koga and J. Nitta, *Phys. Rev.* **B 70**, 201307 (2004).
55. D. M. Zumbühl, J. B. Miller, C. M. Marcus, D. Goldhaber-Gordon, J. S. Harris, K. Campman and A. C. Gossard, *Phys. Rev.* **B 72**, 081305R (2005).